



HAL
open science

Terahertz emission from laser-driven gas-plasmas: a plasmonic point of view

I. Thiele, B. Zhou, A. Nguyen, E. Smetanina, R. Nuter, P González de Alaiza Martínez, K. J. J Kaltenecker, J. Déchard, L Bergé, P. U. U Jepsen, et al.

► To cite this version:

I. Thiele, B. Zhou, A. Nguyen, E. Smetanina, R. Nuter, et al.. Terahertz emission from laser-driven gas-plasmas: a plasmonic point of view. 2018. hal-01737961v1

HAL Id: hal-01737961

<https://hal.science/hal-01737961v1>

Preprint submitted on 20 Mar 2018 (v1), last revised 8 Jan 2019 (v2)

HAL is a multi-disciplinary open access archive for the deposit and dissemination of scientific research documents, whether they are published or not. The documents may come from teaching and research institutions in France or abroad, or from public or private research centers.

L'archive ouverte pluridisciplinaire **HAL**, est destinée au dépôt et à la diffusion de documents scientifiques de niveau recherche, publiés ou non, émanant des établissements d'enseignement et de recherche français ou étrangers, des laboratoires publics ou privés.

Terahertz emission from laser-driven gas-plasmas: a plasmonic point of view

I. Thiele,^{1,2,*} B. Zhou,³ A. Nguyen,⁴ E. Smetanina,^{1,5} R. Nuter,¹ P. González de Alaiza Martínez,¹ K. J. Kaltenecker,³ J. Déchard,⁴ L. Bergé,⁴ P. U. Jepsen,³ and S. Skupin^{1,6}

¹Univ. Bordeaux - CNRS - CEA, Centre Lasers Intenses et Applications, UMR 5107, 33405 Talence, France

²Department of Physics, Chalmers University of Technology, SE-412 96 Göteborg, Sweden

³DTU Fotonik/Department of Photonics Engineering,

Technical University of Denmark, DK-2800 Kongens Lyngby, Denmark

⁴CEA/DAM Île-de-France, Bruyères-le-Châtel, 91297 Arpajon, France

⁵Department of Physics, University of Gothenburg, SE-412 96 Göteborg, Sweden

⁶Institut Lumière Matière, UMR 5306 Université Lyon 1 - CNRS, Université de Lyon, 69622 Villeurbanne, France

(Dated: March 20, 2018)

We investigate terahertz generation in two-color laser-induced gas plasmas. Resonances attributed to plasmonic effects are shown to broaden the emission spectra significantly, when electrons are excited along a direction where the plasma size is smaller than the plasma wavelength. We demonstrate that such resonances can be turned on and off by changing the polarization properties of elliptically-shaped driving laser-pulses. Both 3D Maxwell consistent simulations and experimental results confirm that a significant THz pulse shortening and spectral broadening can be achieved by exploiting the transverse driving laser-beam shape as an additional degree of freedom.

Terahertz (THz) radiation has become an ubiquitous tool for many applications in science and technology [1, 2]. Quite a number of those applications, as for example THz time-domain spectroscopy, require broadband THz sources. Unlike conventional THz sources such as photo-conductive switches [2] or quantum cascade lasers [3], laser-induced gas-plasmas straightforwardly produce emission from THz up to far-infrared frequencies [4]. In the standard setup, a femtosecond (fs) two-color (2C) laser pulse composed of fundamental harmonic (FH) and second harmonic frequency (SH) is focused into an initially neutral gas creating free electrons via tunnel ionization. These electrons are accelerated by the laser electric field and produce a macroscopic current leading to THz emission.

Numerous experimental results show that the laser-induced free electron density has a strong impact on the THz emission spectra [4–8]. This allows for tunability when the THz spectrum is broadened with increasing gas pressure. However, the role of the free electron density remains controversial. In [5, 7, 8], homogeneous plasma oscillations were proposed as an explanation for the observed broadband THz emission, even though those oscillations are in principle non-radiative [9–14]. Moreover, nonlinear propagation effects have been held responsible for the THz spectral broadening as well [6, 15].

On the other hand, the gas plasma produced by the fs laser pulse is a finite conducting structure with a lifetime largely exceeding the fs time scale. Thus, one can expect that the gas plasma features plasmonic resonances which may have a strong impact on the THz emission properties. Similar effects are frequently exploited in the context of plasmonic nanoantennas (or metamaterials), e.g. for SH generation [16], where tailoring such resonances

by tuning the shape of the plasmonic particle is a standard approach. However, it seems that plasmonic effects in the THz emitting gas plasmas were so far completely overlooked, in particular when it comes to active control over the emission properties.

In this letter, we consider the 2C-laser-induced plasma as a plasmonic structure. By using elliptically shaped laser beams, it is possible to turn on and off the THz plasmonic resonances (see Fig. 1). Depending on whether the laser polarization is oriented along the long beam axis (quasi transverse electric, qTE) or along the short beam axis (quasi transverse magnetic, qTM), plasmon-polariton-like resonances are triggered or not. We show by means of three-dimensional (3D) Maxwell consistent simulations in tightly focused geometry that these plas-

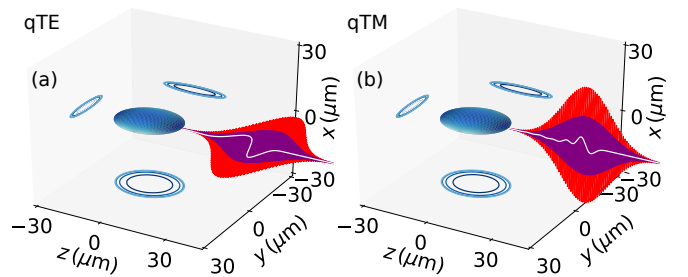


FIG. 1. Illustrated configurations of THz emission from an ellipsoidal plasma induced by a 2C Gaussian laser pulse (FH in red, SH in purple) with strongly elliptical beam shape propagating along z . The laser electric field is y -polarized (along the long axis of the beam, qTE) in (a) and x -polarized (along the short axis, qTM) in (b). The plasma is sketched as blue surface. Simulated forward emitted THz pulses recorded at $z = 12.7 \mu\text{m}$ behind the plasma are presented as white lines demonstrating a significantly shorter pulse duration for qTM polarization, which can be attributed to triggering a plasmonic resonance ($E_\omega = 40 \text{ GV/m}$, $E_{2\omega} = 20 \text{ GV/m}$, $t_0 = 50 \text{ fs}$, $w_{0,x} = \lambda_{\text{FH}} = 0.8 \mu\text{m}$, $w_{0,y} = 8 \mu\text{m}$).

* illia-thiele@web.de

monic resonances indeed broaden the THz spectrum emitted from a microplasma significantly. Finally, we confirm experimentally that this effect is significant also under weaker focusing conditions and for larger plasmas.

Throughout this paper the driving laser pulse is defined by its transverse vacuum electric field at focus,

$$\mathbf{E}_{L,\perp}(\mathbf{r}_\perp, z=0, t) = \exp\left(-\frac{x^2}{w_{0,x}^2} - \frac{y^2}{w_{0,y}^2} - \frac{t^2}{t_0^2}\right) \times \left[E_\omega \cos(\omega_L t) + E_{2\omega} \cos(2\omega_L t + \phi) \right] \mathbf{e}_L, \quad (1)$$

where $\mathbf{r}_\perp = (x, y)^T$ and z are the transverse and longitudinal spatial coordinates, t is the time, t_0 the pulse duration, $w_{0,x}$ the short and $w_{0,y}$ the long vacuum focal beam width, $E_\omega, E_{2\omega}$ the FH or SH electric field amplitudes, $\omega_L = 2\pi c/\lambda_L$ the FH laser frequency with wavelength λ_L , ϕ the relative phase angle, and the unit vector \mathbf{e}_L defines the (linear) laser polarization direction. The laser pulse propagates in the positive z direction, and the origin of the coordinate system is chosen at the vacuum focal point. By defining the tightly focused laser pulse at vacuum focus we follow the algorithm described in [17].

For 2C-driving laser pulses and laser intensities of $10^{14} - 10^{16}$ W/cm², the ionization current (IC) mechanism is responsible for THz generation in gas-plasmas [4]. Thus, the THz-emitting current \mathbf{J} is given by

$$\partial_t \mathbf{J} + \nu_{ei} \mathbf{J} = \frac{q_e^2}{m_e} n_e \mathbf{E}, \quad (2)$$

with electron charge q_e , mass m_e and electric field \mathbf{E} . The electron density n_e is computed by means of rate equations employing a tunnel ionization rate [18, 19], and the electron-ion collision frequency ν_{ei} depends on the ion densities and the electron energy density [20]. This model also appears as the lowest order of the expansion developed in [10], and fully comprises the IC mechanism [21]. In App. A, we briefly review this model that is solved by our code ARCTIC which is benchmarked against more rigorous particle-in-cell simulations in [21].

The laser pulse parameters in Fig. 1 and in the following simulations are chosen such that in argon with initial neutral density $n_a = 3 \times 10^{19}$ cm⁻³ (≈ 1 bar) a fully singly ionized ellipsoidal plasma is created (see App. B). The peak electron density $n_e^{\max} = n_a$ translates into a maximum plasma frequency $\nu_p^{\max} = \sqrt{\frac{n_a q_e^2}{m_e \epsilon_0}} / (2\pi) \approx 50$ THz and a minimum plasma wavelength $\lambda_p^{\min} = c/\nu_p^{\max} \approx 6$ μ m. As visualized in Fig. 1, the transverse plasma profile is strongly elliptical, that is, along x direction the plasma size is less than 1 μ m, whereas along y direction the plasma is approximately 10 μ m wide. By setting the linear laser polarization $\mathbf{e}_L = \mathbf{e}_y$ (qTE) or $\mathbf{e}_L = \mathbf{e}_x$ (qTM), we thus excite a THz emitting current \mathbf{J} along y direction where the plasma profile is wide and electron density gradients are weak or along x direction where the plasma profile is narrow and electron density gradients are strong.

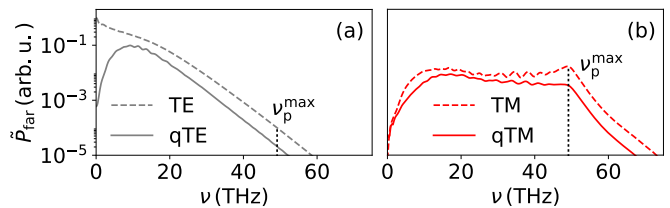


FIG. 2. Angularly integrated far-field spectra for the elliptical beams from Fig. 1 (solid lines) and corresponding results from 2D simulations assuming translational invariance in y (dashed lines).

Considering the forward emitted THz radiation in Fig. 1, we find strong single-cycle pulses reaching field amplitudes of 10 kV/cm. Most importantly, the THz pulse obtained for qTM (b) is two times shorter than for qTE (a), as a direct consequence of the THz emission spectra that are dramatically different. 3D angularly integrated THz far-field spectra are presented in Fig. 2, and for qTM polarization the THz spectrum is broadened up to about 50 THz, the maximum plasma frequency ν_p^{\max} , while for qTE polarization no such broadening is found. The total THz pulse energy ($\nu < 70$ THz) for qTE is 4.8 times larger than for qTM.

Before performing a more detailed theoretical analysis, let us give a simple explanation for the difference in the THz spectra for qTE and qTM polarization: When the plasma current is excited along the direction of weak plasma gradients, the charge separation created due to the displacement of the electrons with respect to the ions is relatively small. Thus, the restoring force is small and the electron current can persist for a long time which leads to a quasi-DC current resulting in the emission of rather low frequencies. In contrast, when the plasma current is excited along the direction of strong plasma gradients, a significant charge separation force pulls the electrons back to the ions resulting in higher frequency components in the current and the emitted radiation.

The dashed lines in Fig. 2 show the results of corresponding 2D simulations, i.e., $w_{0,y} \rightarrow \infty$ when assuming translational invariance along y . In this limit, we find a similar behavior: no broadening if the laser electric field is oriented in the now translationally invariant y direction (transverse electric TE), and broadening up to ν_p^{\max} if the laser electric field points in the direction of the strong electron density gradient, that is, along the x direction (transverse magnetic TM). The TE polarization state governs the field components B_x, E_y, B_z , and the TM polarization state governs the field components E_x, B_y, E_z . Any other polarization state in 2D geometry can be written as the superposition of these two cases, provided that the plasma density remains unchanged. We checked that this property also holds for 3D elliptical beams (see App. B for details). This possibility of superposing qTE and qTM polarization implies that the THz emission spectrum can be tuned by rotating the linear polarization of the incoming laser pulse.

In the following, we want to give a more detailed analysis of the reduced 2D system and explain the difference in the THz spectra for TE and TM pump laser polarization. To this end, we resort to a simple plasma slab model that is detailed in App. C. In short, we consider a system as sketched in Fig. 3(a): A plasma slab with thickness d along the x -direction characterized by a time-invariant electron density n_0 and collision frequency ν_{ei} . Both quantities are assumed to be translational invariant in y and z . Above and below the slab we assume a semi-infinite vacuum. We split the electric field according to $\mathbf{E} = \tilde{\mathbf{E}} + \mathbf{E}_L$, where $\tilde{\mathbf{E}}$ is the field due to interaction of the laser with the plasma and \mathbf{E}_L is the laser field defined by its propagation in vacuum. Then, the right-hand-side of Eq. (C1) reads $\frac{q_e^2}{m_e} n_e \tilde{\mathbf{E}} + \frac{q_e^2}{m_e} n_e \mathbf{E}_L$. The trick is now to replace in the first term the time-dependent electron density n_e by the time-invariant electron density n_0 in order to be able to use a simple analytical expression for the slab response. In the second (THz source) term we keep the time dependent $n_e(t)$ accounting for ionization by the laser. By doing so, we consider the plasma slab to be excited by the current source $\boldsymbol{\iota} = \frac{q_e^2}{m_e} n_e \mathbf{E}_L$. We further approximate this source term by using 2D paraxial laser field propagation and the corresponding time and z

dependent electron density on the optical axis. Such current source $\boldsymbol{\iota}$ is presented in Fig. 3(b) in temporal and longitudinal spatial Fourier space with variables ω and k_z , in the following denoted by "vv". Furthermore, we assume $\boldsymbol{\iota}$ to be invariant along x inside the slab and zero outside. Under these approximations, the solution $\tilde{\mathbf{E}}$ can be obtained straightforwardly. For TE polarization, the y component of the electric field in the vacuum above the slab $x > d/2$ reads

$$\check{\check{E}}_y^v = \frac{i\omega\check{Q}_y}{(\Lambda^p)^2} \left[\frac{\Lambda^v}{D^p} \cosh\left(\frac{\Lambda^p d}{2}\right) + 1 \right] e^{\mp\Lambda^v(x-\frac{d}{2})}, \quad (3)$$

with $\Lambda^v = \sqrt{k_z^2 - \omega^2/c^2}$, $\Lambda^p = \sqrt{k_z^2 - \epsilon^p \omega^2/c^2}$, plasma dispersion $\epsilon^p = 1 - \omega_p^2/(\omega^2 + i\omega\nu_{ei})$, and

$$D^p = \mp\alpha_{TE}\Lambda^p \sinh\left(\frac{\Lambda^p d}{2}\right) - \Lambda^v \cosh\left(\frac{\Lambda^p d}{2}\right). \quad (4)$$

Here, for $k_z^2 \geq \omega^2/c^2$ we use the upper sign in Eqs. (3) and (4), and the lower sign otherwise. The source term \check{Q}_y follows from $\check{Q} = \mu_0 \check{\boldsymbol{\iota}}/(-i\omega + \nu_{ei})$ and involves the transverse laser electric field component (here y), and $\alpha_{TE} = 1$. The field inside the plasma slab is given by

$$\check{\check{E}}_y^p = \frac{i\omega\check{Q}_y}{(\Lambda^p)^2} \left[\frac{\Lambda^v}{D^p} \cosh(\Lambda^p x) + 1 \right]. \quad (5)$$

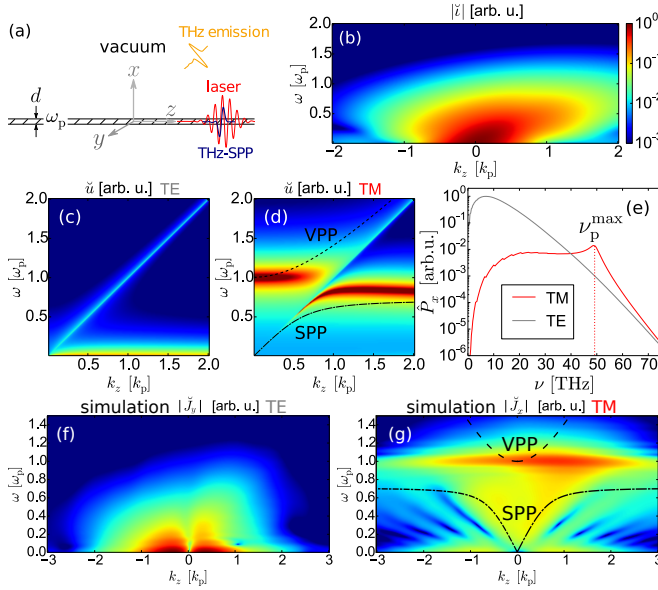


FIG. 3. (a) Illustration of the plasma slab model. (b) Model excitation spectrum of a 2D 2C-laser pulse. Spectral energy in the slab for a (k_z, ω) -independent excitation for TE (c) and TM (d). (e) Far-field spectra for TE and TM predicted by the plasma slab model for excitation spectrum (b), reproducing well 2D and 3D simulation results from Fig. 2. Spectral current amplitudes from 2D simulations for TE (f) and TM (g). The color bar in (b) is valid for all color plots. The slab thickness is $d = 0.4 \mu\text{m}$, the plasma frequency $\omega_p/(2\pi) = \nu_p = 49.15 \text{ THz}$ and the collision frequency $\nu_{ei} = 13 \text{ ps}^{-1}$. In (d,g) the volume-plasmon-polariton (VPP) and surface-plasmon-polariton (SPP) dispersion relations of a single plasma-vacuum interface are indicated.

In order to compute $\check{\check{B}}_y$ for TM polarization, we use the same expressions after replacing $\omega\check{Q}_y$ by $k_z\check{Q}_x$ (now the driving laser is x polarized) and α_{TE} by $\alpha_{TM} = 1/\epsilon_p$ in Eqs. (3)-(5). Fields in the vacuum below the slab $x < -d/2$ follow from symmetry considerations.

Let us first examine the response of the plasma slab for a (ω, k_z) -independent excitation along y (TE) and x (TM). To this end, we introduce the spectral energy $\check{u} = \int_{-d/2}^{d/2} (\epsilon_0 |\tilde{\mathbf{E}}|^2 + |\tilde{\mathbf{B}}|^2/\mu_0) dx$ inside the slab, presented in Figs. 3(c,d) for TE/TM. Besides the light line $\omega = ck_z$, no particular signatures of resonances can be found for TE in (c). In contrast, surface-plasmon-polariton (SPP)-like and volume-plasmon-polariton (VPP)-like resonances are excited for TM in (d). Those do not follow exactly the dispersion relations of plasmon-polaritons for a single plasma-vacuum interface [22] that are indicated in the graphs, since here we consider a slab with a finite thickness d . The smaller d , the closer those resonances move towards the $\omega(k_z) = \omega_p$ -line (not shown).

Next, we switch to the model current source $\boldsymbol{\iota}$ as shown in Fig. 3(b), and compute the angularly integrated far-field power spectra \hat{P}_x for the 2D plasma slab model. The resulting THz emission spectra are presented in Fig. 3(e) and reproduce well what one obtains from rigorous Maxwell consistent simulations in Fig. 2: In contrast to TE, the emission spectrum for TM polarization is broadened up to the maximum plasma frequency ν_p^{max} .

To confirm that the observed difference between TE and TM indeed originates from a plasmon-polariton-like

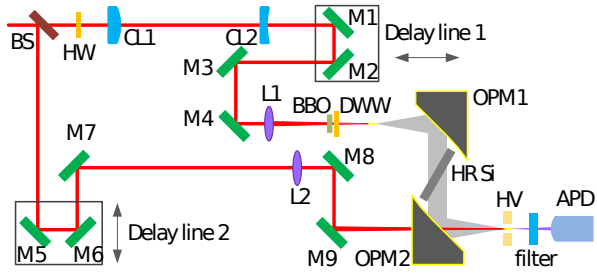


FIG. 4. Sketch for 2C laser-induced air-plasma THz generation and detection system. BS: 800nm Beam splitter; HW: half wave plate; CL1: Plano-Convex cylindrical lens, focal length $f = 1000$ mm; CL2: Plano-Concave cylindrical lens, $f = -400$ mm; M1-9: 45 degree incidence high reflective mirror; Lens L1: $f = 300$ mm; L2: $f = 400$ mm; DWW: Dual wavelength wave plate; OPM1 (OPM2): Off-axis parabolic mirrors, Reflected Focal Length RFL = 4 inch (3 inch); HR Si: high-resistivity Silicon plate; RFL = 3 inch; HV: high voltage; APD: Si Avalanche Photodetector.

structure, we consider the spectral amplitudes of the currents in full 2D simulations in Figs. 3(f,g): Indeed, the plasma-electrons show no feature near ω_p for TE in (f). For TM in (g), we find a resonant excitation around the plasma frequency with similar structures as observed in the response of the slab model in Fig. 3(d).

The (q)TE and (q)TM spectra can thus be explained by the plasma slab model, although small differences occur when directly comparing Figs. 2 and 3(e). We attribute these discrepancies to the fact that in the plasma slab model SPPs cannot couple to radiative modes, and only VPPs can contribute to the far-field emission. However, in reality the plasma has longitudinal truncations that can reflect or transmit SPPs leading to their emission into the far-field as well [16]. Thus, it is likely that SPP- and VPP-like structures fuse in the rigorous simulation [Fig. 3(g)].

So far, we have analyzed the microplasma configuration which relies on strong focusing conditions of the driving laser pulse. In the following, we want to investigate whether plasmonic effects can be observed as well under weaker focusing conditions and higher driving laser-pulse energies leading to longer plasmas. To this end, we resort to a standard experimental setup for two-color laser-induced air plasma THz generation and detection sketched in Fig. 4. The laser pulses originate from a 40 fs, 1 kHz Ti:sapphire regenerative laser amplifier. The average laser power through the beam splitter (pump beam) is 230 mW; and the reflected beam (probe beam) has an average power of 200 mW. The pump beam is vertically polarized by a half wave plate (800 nm) and sent into a 100- μm -thick BBO crystal through a 300-mm focal lens for second harmonic generation (SHG). The polarization of the fundamental wavelength is then shifted back to horizontal after the SHG process, while the second harmonic wavelength is kept as horizontally polarized. Off-axis parabolic mirrors are used to collimate and focus

the THz field. A piece of high-resistivity silicon plate is employed to block the residual FH and SH laser beam. The probe beam, meanwhile, is focused by lens L2 and overlapped with the focus of the THz field through a central hole in OPM2. The detection of the THz waveform is done by using the so-called air-biased coherent detection scheme [23] where in the presence of the THz field the four-wave-mixing-generated SH of the probe beam is measured. An avalanche photodiode (APD) is employed as photodetector. A boxcar integrator is then necessary to reshape the fast APD response (few ns) before it can be picked up by the lock-in amplifier. The part of the setup where THz waves are involved is covered by a plastic box and purged with dry nitrogen during the measurements. A pair of cylindrical lenses is employed in the pump beam arm to elliptically shape the otherwise near-Gaussian pump beam profile. We rotate both cylindrical lenses by 90° to switch the pump electric field mode between qTE and qTM. The probe beam arm, on the other hand, is kept the same to ensure identical probe condition for THz generated by different pump beam modes.

The experimental 2C elliptical beam creates an about 25-mm-long plasma for any rotation angle of the cylindrical lenses. By simulating the laser propagation by means of the unidirectional pulse propagation equation [24], we could estimate the peak electron density to $1.2 \cdot 10^{18} \text{ cm}^{-3}$ corresponding to the maximum plasma frequency $\nu_p^{\text{max}} = 9.9 \text{ THz}$, and transverse FWHM extensions of the elliptical plasma of 20 μm and 54 μm .

The experimentally detected THz spectra and waveforms are presented in Fig. 5. The THz pulse duration for qTM polarization is about 1.6 times shorter than for qTE. A pyroelectric measurement revealed a THz pulse energy ratio between qTE and qTM of 2.5. In full agreement with our theoretical results, the qTM spectrum is significantly broader than the qTE spectrum. Moreover, the maximum THz emission for qTM is found at the estimated maximum plasma frequency (dashed line). Thus, our experimental results support the hypothesis that the plasmon-polariton-like resonances broaden the THz spectrum, even for longer plasmas and larger beam widths.

In summary, we have shown that plasmonic effects can significantly broaden the terahertz emission spectrum

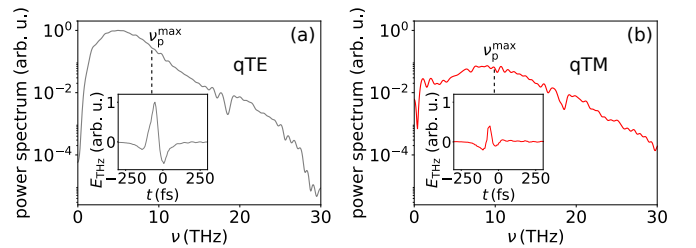


FIG. 5. Experimental THz spectra for qTE (a) and qTM (b) polarization (see text for details). Corresponding on-axis THz waveforms are shown as insets. The dashed lines specify the estimated maximum plasma frequency.

from fs-laser-induced gas-plasmas when the corresponding wavelengths are larger than the plasma size, that is, electron density gradients are sufficiently steep. We propose an efficient THz-generation scheme to access this effect by two-color elliptically-shaped laser-beam-induced gas-plasmas via the ionization current mechanism and demonstrate its experimental feasibility. Turning the polarization of the excitation, when adjusting the linear laser polarization, we can switch THz spectral broadening due to plasmonic resonances on or off and thus control the THz emission spectrum. This plasmonic view on gas-plasma-based THz generation paves a way towards resonant control of THz generation. We believe that our results, which are a priori not limited to the gas-plasma configuration, will trigger further experimental and theoretical efforts in this direction.

Numerical simulations were performed using computing resources at Mésocentre de Calcul Intensif Aquitaine (MCIA) and Grand Équipement National pour le Calcul Intensif (GENCI, Grants No. 2016-056129, No. 2016-057594, No. A0020507594 and No. A0010506129). This study was supported by ANR (Projet ALTESSE). S.S. acknowledges support by the Qatar National Research Fund through the National Priorities Research Program (Grant No. NPRP 8-246-1-060).

Appendix A: Modeling the ionization current mechanism for microplasmas

The THz generation by two-color laser pulses considered here is driven by the so-called ionization current (IC) mechanism [4]. A comprehensive model based on the fluid equations for electrons describing THz emission has been derived in [10]. In this framework, the IC mechanism naturally appears at the lowest order of a multiple-scale expansion. Besides the IC mechanism, this model is also able to treat THz generation driven by ponderomotive forces and others. They appear at higher orders of the multiple-scale expansion and are not considered here. In the following, we briefly summarize the equations describing the IC mechanism.

The electromagnetic fields \mathbf{E} and \mathbf{B} are governed by Maxwell's equations in vacuum

$$\nabla \times \mathbf{E} = -\partial_t \mathbf{B}, \quad (\text{A1})$$

$$\nabla \times \mathbf{B} = \frac{1}{c^2} \partial_t \mathbf{E} + \mu_0 \mathbf{J} + \mu_0 \mathbf{J}_{\text{loss}}. \quad (\text{A2})$$

The plasma and electromagnetic fields are coupled via the conductive current density \mathbf{J} governed by

$$\partial_t \mathbf{J} + \nu_{\text{ei}} \mathbf{J} = \frac{q_e^2}{m_e} n_e \mathbf{E}, \quad (\text{A3})$$

where electron-ion collisions lead to a damping of the current. The collision frequency is determined by [20]

$$\nu_{\text{ei}} [\text{s}^{-1}] = \frac{3.9 \times 10^{-6} \sum_Z Z^2 n_{\text{ion}}^{(Z)} [\text{cm}^{-3}] \lambda_{\text{ei}}}{E_{\text{elec}} [\text{eV}]^{3/2}}, \quad (\text{A4})$$

where λ_{ei} is the Coulomb logarithm. The value $\lambda_{\text{ei}} = 3.5$ turned out to match the results obtained by more sophisticated calculations with Particle-In-Cell (PIC) codes in [10]. The densities of Z times charged ions are determined by a set of rate equations

$$\begin{aligned} \partial_t n_{\text{ion}}^{(Z)} &= W^{(Z)} n_{\text{ion}}^{(Z-1)} - W^{(Z+1)} n_{\text{ion}}^{(Z)} \\ \partial_t n_{\text{ion}}^{(0)} &= -W^{(1)} n_{\text{ion}}^{(0)} \end{aligned} \quad (\text{A5})$$

for $Z = 1, 2, 3, \dots, K$, and the initial neutral density is $n_{\text{ion}}^{(0)}(t = -\infty) = n_a$. The tunnel ionization rate $W^{(Z)}$ in quasi-static approximation creating ions with charge Z is taken from [18, 19]. Thus, $W^{(Z)}$ is a function of the modulus of the electric field \mathbf{E} . The atoms can be at most K times ionized and thus $W^{(K+1)} = 0$. The electron density is determined by the ion densities

$$n_e = \sum_Z Z n_{\text{ion}}^{(Z)}. \quad (\text{A6})$$

The electron energy density $\mathcal{E} = n_e E_{\text{elec}}$ is governed by

$$\partial_t \mathcal{E} = \mathbf{J} \cdot \mathbf{E}. \quad (\text{A7})$$

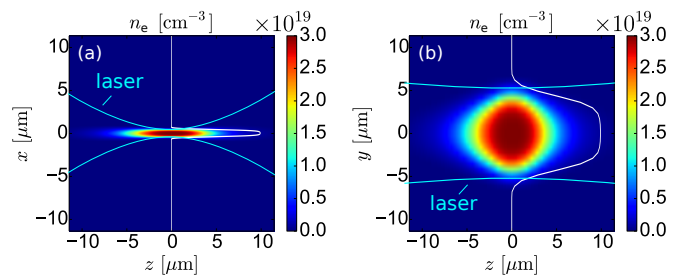


FIG. 6. Electron density in (a) zx and (b) yz planes after ionization of an Argon gas with initial neutral density $n_a = 3 \times 10^{19} \text{ cm}^{-3}$ ($\approx 1 \text{ bar}$) by a 2C elliptically shaped laser pulse ($E_\omega = 40 \text{ GV/m}$, $E_{2\omega} = 20 \text{ GV/m}$, $t_0 = 50 \text{ fs}$, $w_{0,x} = \lambda_{\text{FH}} = 0.8 \text{ }\mu\text{m}$, $w_{0,y} = 8 \text{ }\mu\text{m}$, see the main article for definition of the parameters). The respective electron density profiles at focus ($z = 0$) are visualized by the bright white lines. The waist of the focused laser is tracked by the light blue lines.

The loss current accounting for ionization losses in the laser field reads

$$\mathbf{J}_{\text{loss}} = \frac{\mathbf{E}}{|\mathbf{E}|^2} \sum_Z I_p^Z W^{(Z)} n_{\text{ion}}^{(Z-1)}, \quad (\text{A8})$$

where I_p^Z is the ionization potential for creation of an ion with charge Z . Even though ionization losses as well as higher order ionization ($Z = 2, 3, \dots$) are negligible in the framework of the present study, both are kept for completeness.

The model is implemented in the code ARCTIC, that solves Eqs. (A1)-(A2) by means of the Yee scheme [25]. We have previously benchmarked the code ARCTIC by the PIC code OCEAN accounting for full kinetics of the plasma [26] in [21].

Appendix B: THz emission from elliptically shaped microplasmas

In the main article we investigate terahertz (THz) emission from elliptically shaped two-color (2C)-laser-induced gas-plasmas. In such a configuration, the free electron density profile with a small transverse size along x and a large transverse size along y is created. As can be seen from Fig. 6, for the considered microplasmas the transverse plasma profile is strongly elliptical, that is, along x direction the plasma size is less than $1 \text{ }\mu\text{m}$, whereas along y direction the plasma is approximately $10 \text{ }\mu\text{m}$ wide. As can be seen from the transverse electron density profiles (bright white lines), the electron density gradients are large along x and significantly smaller along y . Thus, by rotating the linear laser electric field polarization with respect to the transverse plasma profile, we can select the strength of the electron density gradients along the excitation direction.

As can be seen in the 3D angularly integrated far-field spectra presented in Fig. 7, when exciting the plasma

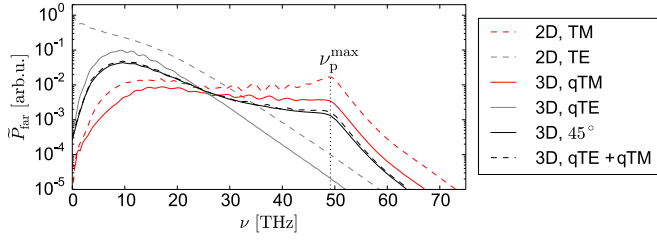


FIG. 7. Angularly integrated far-field spectra for the elliptical beams from Figs. 6 (solid lines) and corresponding results from 2D simulations assuming translational invariance in y (dashed lines). The solid black line specifies the emission spectrum from a 3D simulation with laser polarization at 45° in the xy plane. The dashed black line is computed from the superimposed fields of the qTM and qTE cases in 3D.

along strong electron density gradients (qTM, dark red solid line), the THz spectrum is broadened up to about 50 THz, which corresponds to the maximum plasma frequency ν_p^{\max} . In contrast, when exciting the plasma along the weak electron density gradients (qTE) no such broadening is found (light gray solid line). Results of corresponding 2D simulations ($\partial_y = 0$) are shown as dashed lines. Here, we find a similar behavior: no broadening if the laser electric field is oriented in the now translationally invariant y direction (TE), and broadening up to ν_p^{\max} if the laser electric field points in the direction of the strong electron density gradient, that is, along the x direction (TM). Treating the problem in 2D geometry, i.e., assuming translational invariance in one transverse direction (here y), the electromagnetic fields separate into two cases: the transverse electric (TE) case that governs the fields B_x, E_y, B_z for a y -polarized driving laser pulse and the transverse magnetic (TM) case that governs the fields E_x, B_y, E_z for an x -polarized driving laser pulse. Any other polarization state in 2D can be written as the superposition of these two cases. For example, an incoming laser pulse that is linearly polarized under 45° in the xy plane will give an electric field solution that can be written as $\mathbf{E} = \mathbf{E}^{\text{TE}}/\sqrt{2} + \mathbf{E}^{\text{TM}}/\sqrt{2}$, where \mathbf{E}^{TE} and \mathbf{E}^{TM} are the solutions for a y -(TE) and x -polarized (TM) driving laser pulse, respectively. Therefore, if the 3D elliptical beam can be indeed approximated by the idealized 2D case, and no detrimental nonlinear coupling occurs, this property should hold. We checked this by comparing the angularly integrated THz-far-field power spectrum for a simulation with polarization at 45° (black solid line) and the result for the superposed fields (black dashed line) in Fig. 7. Both overlap almost perfectly, and thus further analysis of the 2D configuration is justified. Moreover, the possibility of superposing qTE and qTM could be important for applications, because it implies that the THz emission spectrum can be tuned by rotating the linear polarization of the incoming laser pulse.

Appendix C: Plasmonic resonances in the plasma slab model

To elaborate the origin of the laser polarization dependence of the THz-emission spectra from elliptically shaped 2C-laser-induced plasmas, we consider a simplified system as sketched in Fig. 3(a) of the main article: A plasma slab of thickness d in x -direction with time-invariant electron density n_0 and collision frequency ν_{ei} . Both quantities are translationally invariant in y and z . Above and below the slab we assume semi-infinite vacuum with constant permittivity $\epsilon^v = 1$. By writing the total electric field as the sum of the laser field \mathbf{E}_L and the field due to laser-plasma interaction $\tilde{\mathbf{E}}$, Eq. (2) in the main article reads as

$$\partial_t \mathbf{J} + \nu_{ei} \mathbf{J} = \frac{q_e^2 n_0}{m_e} \tilde{\mathbf{E}} + \boldsymbol{\iota} \quad (\text{C1})$$

with the source term

$$\boldsymbol{\iota} = \frac{q_e^2 n_e}{m_e} \mathbf{E}_L. \quad (\text{C2})$$

It is important to note that we assume that the source term $\boldsymbol{\iota}$ depends on the product of the laser electric field and the time dependent electron density $n_e(t)$, as it is produced during the laser gas interaction. Only in the description of the response of the plasma slab we make the simplification of a constant density n_0 .

Let us now use Eq. (C1) and Maxwell's equations to determine the response of the system. In frequency space (see App. D for definition), they can be rewritten for angular frequency $\omega \neq 0$ as

$$\nabla \times \hat{\mathbf{E}} = i\omega \hat{\mathbf{B}} \quad (\text{C3})$$

$$\nabla \times \hat{\mathbf{B}} = -i \frac{\omega}{c^2} \epsilon \hat{\mathbf{E}} + \hat{\mathbf{Q}}, \quad (\text{C4})$$

where for sake of brevity we introduced the source term

$$\hat{\mathbf{Q}} = \frac{\mu_0 \hat{\boldsymbol{\iota}}}{-i\omega + \nu_{ei}}. \quad (\text{C5})$$

The dielectric permittivity ϵ reads $\epsilon = \epsilon^P$ in the plasma slab ($|x| \leq d/2$), and $\epsilon = \epsilon^v = 1$ in the vacuum ($|x| > d/2$). The complex dielectric permittivity of the plasma is given by

$$\epsilon^P = 1 - \frac{\omega_p^2}{\omega^2 + i\omega\nu_{ei}}, \quad (\text{C6})$$

where the plasma frequency $\omega_p = \sqrt{\frac{n_0 q_e^2}{m_e \epsilon_0}}$ involves the time independent density n_0 of the slab.

Same as for ϵ , we consider an excitation that is translational invariant in y , that is, $\partial_y \hat{\boldsymbol{\iota}} = 0$ and $\partial_y \hat{\mathbf{Q}} = 0$. Therefore, we can set all the y -derivatives to zero and Eqs. (C3)-(C4) separate into two sets of equations. The translational invariance of the slab in z allows to write

down these two sets of equations in the spatial Fourier domain with respect to z ($\partial_z \rightarrow ik_z$) giving

$$\partial_x \check{E}_y = i\omega \check{B}_z \quad (\text{C7})$$

$$-ik_z \check{E}_y = i\omega \check{B}_x \quad (\text{C8})$$

$$ik_z \check{B}_x - \partial_x \check{B}_z = -i\frac{\omega}{c^2} \epsilon \check{E}_y + \check{Q}_y \quad (\text{C9})$$

and

$$ik_z \check{E}_x - \partial_x \check{E}_z = i\omega \check{B}_y \quad (\text{C10})$$

$$-ik_z \check{B}_y = -i\frac{\omega}{c^2} \epsilon \check{E}_x + \check{Q}_x \quad (\text{C11})$$

$$\partial_x \check{B}_y = -i\frac{\omega}{c^2} \epsilon \check{E}_z + \check{Q}_z, \quad (\text{C12})$$

where “ $\check{\cdot}$ ” indicates the (ω, k_z) -domain according to the definition in App. D. The 1st set of equations (C7)-(C9) is called the transverse electric (TE) case, because the only electric field component E_y is polarized in the transverse translational invariant direction. Here, the only fields different from zero are $(\check{B}_x, \check{E}_y, \check{B}_z)$. The 2nd set of equations (C10)-(C12) is called the TM-case correspondingly and describes the evolution of $(\check{E}_x, \check{B}_y, \check{E}_z)$. In the following, we will consider two different configurations:

(i) TE with transverse excitation in y ($\check{\nu}_y \neq 0 \neq \check{Q}_y$ and $\check{Q}_x = 0 = \check{Q}_z$)

(ii) TM with transverse excitation in x ($\check{\nu}_x \neq 0 \neq \check{Q}_x$ and $\check{Q}_z = 0 = \check{Q}_y$)

Note that (i) corresponds to the THz generation by y -polarized elliptical beams and (ii) by x -polarized elliptical beams as investigated in the main article. In the following, the Maxwell's equations Eqs. (C7)-(C12) for the plasma slab are solved for these two cases.

1. TE with transverse excitation in y

Let us start with case (i), that is, $\check{\nu} = \check{\nu}_y \mathbf{e}_y$. Firstly, the general solutions inside the plasma slab and the neutral gas are computed, and secondly, the continuity of the transverse fields is used to determine the entire solution.

Equations (C7)-(C9) give the evolution equation for the transverse field \check{E}_y inside the plasma and the neutral gas

$$\partial_x^2 \check{E}_y - \left(k_z^2 - \frac{\omega^2}{c^2} \epsilon\right) \check{E}_y = -i\omega \check{Q}_y, \quad (\text{C13})$$

For sake of simplicity, we consider that \check{Q}_y is constant inside the plasma slab and zero outside of it. In particular, this choice makes \check{Q}_y symmetric with respect to x , and \check{E}_y has to obey the same symmetry. Then, the general symmetric solution in the plasma ($|x| \leq d/2$) reads

$$\check{E}_y^{\text{P}} = A^{\text{P}} \cosh(\Lambda^{\text{P}} x) - \frac{i\omega \check{Q}_y}{(\Lambda^{\text{P}})^2} [\cosh(\Lambda^{\text{P}} x) - 1], \quad (\text{C14})$$

where $\Lambda^{\text{P}} = \sqrt{k_z^2 - \epsilon^{\text{P}} \omega^2 / c^2}$. In the vacuum at $x > d/2$ the general solution reads

$$\check{E}_y^{\text{V}} = A^{\text{V}} \exp \left[\mp \Lambda^{\text{V}} \left(x - \frac{d}{2} \right) \right], \quad (\text{C15})$$

where $\Lambda^{\text{V}} = \sqrt{k_z^2 - \omega^2 / c^2}$. For $k_z^2 \geq \omega^2 / c^2$, we use the “-”-sign since for the “+”-sign the field would grow exponentially when $x \rightarrow \infty$. For $k_z^2 < \omega^2 / c^2$, we use the +-sign to obtain only outgoing propagating waves (along x). Note that solution in the vacuum at $x < d/2$ follows from symmetry considerations.

According to Maxwell's interface conditions \check{E}_y, \check{B}_z and thus $\partial_x \check{E}_y$ have to be continuous at the plasma-vacuum interface. These two conditions determine the yet unknown amplitudes A^{P} and A^{V} to

$$A^{\text{P}} = \frac{i\omega \check{Q}_y}{(\Lambda^{\text{P}})^2} \left(\frac{\Lambda^{\text{V}}}{D^{\text{P}}} + 1 \right) \quad (\text{C16})$$

$$A^{\text{V}} = \frac{i\omega \check{Q}_y}{(\Lambda^{\text{P}})^2} \left[\frac{\Lambda^{\text{V}}}{D^{\text{P}}} \cosh \left(\frac{\Lambda^{\text{P}} d}{2} \right) + 1 \right], \quad (\text{C17})$$

with common denominator

$$D^{\text{P}} = \mp \Lambda^{\text{P}} \sinh \left(\frac{\Lambda^{\text{P}} d}{2} \right) - \Lambda^{\text{V}} \cosh \left(\frac{\Lambda^{\text{P}} d}{2} \right). \quad (\text{C18})$$

Finally, Eqs. (C7)-(C8) determine the magnetic field components as

$$\check{B}_x = -\frac{k_z}{\omega} \check{E}_y \quad (\text{C19})$$

$$\check{B}_z^{\text{P}} = \frac{\check{Q}_y}{\Lambda^{\text{P}}} \frac{\Lambda^{\text{V}}}{D^{\text{P}}} \sinh(\Lambda^{\text{P}} x) \quad (\text{C20})$$

$$\check{B}_z^{\text{V}} = \mp \frac{\Lambda^{\text{V}}}{i\omega} A^{\text{V}} \exp \left[\mp \Lambda^{\text{V}} \left(x - \frac{d}{2} \right) \right]. \quad (\text{C21})$$

2. TM with transverse excitation in x

Next, case (ii) with $\check{\nu} = \check{\nu}_x \mathbf{e}_x$ is considered. Equations. (C10)-(C12) give the evolution equation for the transverse field \check{B}_y inside the plasma and neutral gas respectively,

$$\partial_x^2 \check{B}_y - \Lambda^2 \check{B}_y = -ik_z \check{Q}_x. \quad (\text{C22})$$

In analogy to the TE case in the previous section, we obtain in the plasma

$$\check{B}_y^{\text{P}} = A^{\text{P}} \cosh(\Lambda^{\text{P}} x) - \frac{ik_z \check{Q}_x}{(\Lambda^{\text{P}})^2} [\cosh(\Lambda^{\text{P}} x) - 1] \quad (\text{C23})$$

and in upper vacuum

$$\check{B}_y^{\text{V}} = A^{\text{V}} \exp \left[\mp \Lambda^{\text{V}} \left(x - \frac{d}{2} \right) \right]. \quad (\text{C24})$$

The difference to the TE case appears when applying the interface conditions at the plasma-air interface: $\check{\check{B}}_y$ and $\check{\check{E}}_z$ are continuous but according to Eq. (C12) $\partial_x \check{\check{B}}_y$ is not, because ϵ changes at the interface. Applying these TM interface conditions determines A^P and A^V to

$$A^P = \frac{ik_z \check{Q}_x}{(\Lambda^P)^2} \left(\frac{\Lambda^V}{D^P} + 1 \right) \quad (\text{C25})$$

$$A^V = \frac{ik_z \check{Q}_x}{(\Lambda^P)^2} \left[\frac{\Lambda^V}{D^P} \cosh \left(\frac{\Lambda^P d}{2} \right) + 1 \right], \quad (\text{C26})$$

with common denominator

$$D^P = \mp \frac{1}{\epsilon^P} \Lambda^P \sinh \left(\frac{\Lambda^P d}{2} \right) - \Lambda^V \cosh \left(\frac{\Lambda^P d}{2} \right). \quad (\text{C27})$$

Finally, Eqs. (C11)-(C12) determine the electric field components as

$$\check{\check{E}}_x = \frac{k_z c^2}{\omega \epsilon} \check{\check{B}}_y - \frac{ic^2}{\omega \epsilon} \check{Q}_x \quad (\text{C28})$$

$$\check{\check{E}}_z^P = -\frac{k_z \check{Q}_x c^2}{\omega \epsilon^P \Lambda^P} \frac{\Lambda^V}{D^P} \sinh(\Lambda^P x) \quad (\text{C29})$$

$$\check{\check{E}}_z^V = \mp \frac{ic^2 \Lambda^V}{\omega} A^V \exp \left[\mp \Lambda^V \left(x - \frac{d}{2} \right) \right]. \quad (\text{C30})$$

3. Model current source term

In the previous calculations, we have assumed that the current source term is constant along x in the slab and zero in vacuum. In order to approximate its z dependency, we need a z dependent electric laser field. To this end, we use the electric field on the optical axis in quasi-monochromatic 2D paraxial approximation with

$$\begin{aligned} \mathbf{E}_L^{\text{mod}}(z, t) \approx \Re \left\{ \frac{E_\omega e^{-\frac{(t-z/c)^2}{t_0^2} - i\omega_L(t-z/c)}}}{\sqrt{1 + i \frac{z}{z_R(\omega_L)}}} \right\} \mathbf{e}_L \\ + \Re \left\{ \frac{E_{2\omega} e^{-\frac{(t-z/c)^2}{t_0^2} - i2\omega_L(t-z/c)}}}{\sqrt{1 + i \frac{z}{z_R(2\omega_L)}}} \right\} \mathbf{e}_L, \end{aligned} \quad (\text{C31})$$

where $z_R(\omega) = \omega_0^2 x \omega / 2c$ is the Rayleigh length, the symbol \Re denotes the real part of a complex quantity and all other quantities are defined as in the main article. Then the model current source in the slab reads

$$\boldsymbol{\iota}^{\text{mod}} = \frac{q_e^2 n_e [\mathbf{E}_L^{\text{mod}}]}{m_e} \mathbf{E}_L^{\text{mod}}. \quad (\text{C32})$$

This current source is displayed in Fig. 3(b) of the main article, and was used to compute Fig. 3(e).

Appendix D: Fourier transforms

In the following, we define the temporal Fourier transform $\hat{f}(\mathbf{r}, \omega)$ of a function $f(\mathbf{r}, t)$ by

$$\hat{f}(\mathbf{r}, \omega) = \frac{1}{2\pi} \int f(\mathbf{r}, t) e^{i\omega t} dt \quad (\text{D1})$$

$$f(\mathbf{r}, t) = \int \hat{f}(\mathbf{r}, \omega) e^{-i\omega t} d\omega. \quad (\text{D2})$$

Furthermore, we define the longitudinal spatial Fourier transform $\check{f}(\mathbf{r}_\perp, k_z, \omega)$ of a function $\hat{f}(\mathbf{r}, \omega)$ by

$$\check{f}(\mathbf{r}_\perp, k_z, \omega) = \frac{1}{2\pi} \int \hat{f}(\mathbf{r}_\perp, z, \omega) e^{-ik_z z} dz \quad (\text{D3})$$

$$\hat{f}(\mathbf{r}_\perp, z, \omega) = \int \check{f}(\mathbf{r}_\perp, k_z, \omega) e^{ik_z z} dz. \quad (\text{D4})$$

Note the difference in the sign of the exponent for temporal and spatial transforms, which is common practice in the optical context.

1. Far-field spectra

We introduce the spectral poynting flux

$$\check{\mathbf{S}} = 2/\mu_0 \Re \{ \check{\mathbf{E}} \times \check{\mathbf{B}}^* \}. \quad (\text{D5})$$

The angularly integrated far-field spectrum \hat{P}_x can be obtained by integrating $\check{\mathbf{S}}$ along k_z .

Appendix E: Results of the unidirectional pulse propagation equation approach

In the main article, we have used for the estimation of the maximum electron density under the underlying experimental conditions the simulation results of the unidirectional propagation equation (UPPE) approach [24]. Here, we want to discuss the results of this simulation which are presented in Fig. 8 in more detail.

As can be seen in Fig. 8(a), the laser beam is focused after about 5 cm. Before the focus, the elliptical beam is wider along x than y [see Fig. 8(b)]. In the focal plane, the elliptical beam profile rotates and the beam is wider along y than x [see Fig. 8(c)]. The 230 μJ of laser pulse energy create a 2.5-cm-long plasma [see Fig. 8(a)]. The peak electron density grows to $n_p^{\text{max}} = 1.2 \cdot 10^{18} \text{ cm}^{-3}$ which corresponds to the maximum plasma frequency $\nu_e^{\text{max}} = \sqrt{q_e^2 n_e^{\text{max}} / (m_e \epsilon_0)} / (2\pi) = 9.9 \text{ THz}$. The transverse plasma shape is strongly elliptical [see Fig. 8(d)].

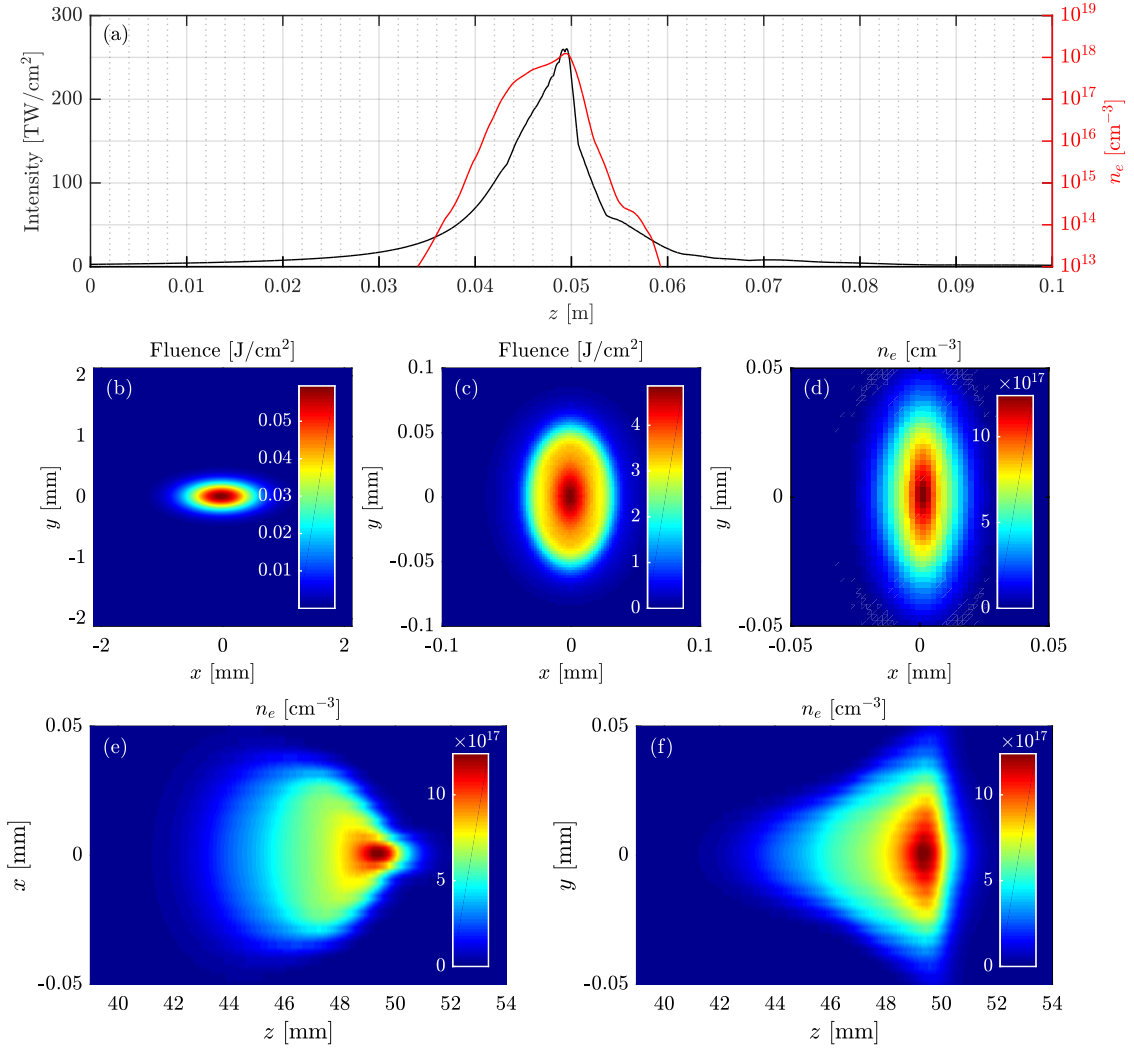


FIG. 8. Results of the UPPE simulation: (a) Peak intensity (black dashed line) and the electron density (red solid line) along the propagation. (b) Fluence before the focus at $z = 0$. (c) Fluence in the focal plane at $z = 0.05$ m. (d) Electron density profile in focus at $z = 0.05$ m. (e) Electron density profile in the xz -plane ($y = 0$). (f) Electron density profile in the yz -plane ($x = 0$).

-
- [1] T. Kampfrath, K. Tanaka, and K. A. Nelson, *Nat. Photon.* **7**, 680 (2013).
- [2] M. Tonouchi, *Nat. Photon.* **1**, 97 (2007).
- [3] M. S. Vitiello, G. Scalari, B. Williams, and P. D. Natale, *Opt. Express* **23**, 5167 (2015).
- [4] K. Y. Kim, A. J. Taylor, S. L. Chin, and G. Rodriguez, *Nat. Photon.* **2**, 605 (2008).
- [5] H. Hamster, A. Sullivan, S. Gordon, and R. W. Falcone, *Phys. Rev. E* **49**, 671 (1994).
- [6] I. Babushkin, W. Kuehn, C. Köhler, S. Skupin, L. Bergé, K. Reimann, M. Woerner, J. Herrmann, and T. Elsaesser, *Phys. Rev. Lett.* **105**, 053903 (2010).
- [7] N. Li, Y. Bai, T. Miao, P. Liu, R. Li, and Z. Xu, *Opt. Express* **24**, 23009 (2016).
- [8] V. A. Andreeva, O. G. Kosareva, N. A. Panov, D. E. Shipilo, P. M. Solyankin, M. N. Esaulkov, P. González de Alaiza Martínez, A. P. Shkurinov, V. A. Makarov, L. Bergé, and S. L. Chin, *Phys. Rev. Lett.* **116**, 063902 (2016).
- [9] V. T. Tikhonchuk, *Phys. Rev. Lett.* **89**, 209301 (2002).
- [10] I. Thiele, R. Nuter, B. Bousquet, V. Tikhonchuk, S. Skupin, X. Davoine, L. Gremillet, and L. Bergé, *Phys. Rev. E* **94**, 063202 (2016).
- [11] P. Sprangle, J. R. Peñano, B. Hafizi, and C. A. Kapetanacos, *Phys. Rev. E* **69**, 066415 (2004).
- [12] L. M. Gorbunov and A. A. Frolov, *Plasma Physics Reports* **32**, 850 (2006).
- [13] P. González de Alaiza Martínez, X. Davoine, A. Debayle, L. Gremillet, and L. Bergé, *Scientific Reports* **6**, 26743 (2016).
- [14] C. Miao, J. P. Palastro, and T. M. Antonsen, *Physics of Plasmas* **23**, 063103 (2016).
- [15] E. Cabrera-Granado, Y. Chen, I. Babushkin, L. Bergé, and S. Skupin, *New J. Phys.* **17**, 023060 (2015).
- [16] S. B. Hasan, C. Etrich, R. Filter, C. Rockstuhl, and F. Lederer, *Phys. Rev. B* **88**, 205125 (2013).
- [17] I. Thiele, S. Skupin, and R. Nuter, *Journal of Computational Physics* **321**, 1110 (2016).
- [18] M. Ammosov, N. Delone, and V. Krainov, *Sov. Phys. JETP* **64**, 1191 (1986).
- [19] G. L. Yudin and M. Y. Ivanov, *Phys. Rev. A* **64**, 013409 (2001).
- [20] J. D. Huba, *Plasma Physics* (Naval Research Laboratory, Washington, DC, 2013).
- [21] I. Thiele, P. González de Alaiza Martínez, R. Nuter, A. Nguyen, L. Bergé, and S. Skupin, *Phys. Rev. A* **96**, 053814 (2017).
- [22] S. A. Maier, *Plasmonics: Fundamentals and Applications*, 3rd ed. (Springer, 1999).
- [23] J. Dai, X. Xie, and X.-C. Zhang, *Phys. Rev. Lett.* **97**, 103903 (2006).
- [24] M. Kolesik and J. V. Moloney, *Phys. Rev. E* **70**, 036604 (2004).
- [25] K. S. Yee, *IEEE Trans. Antennas Propagat.* **AP-14**, 302 (1966).
- [26] R. Nuter and V. Tikhonchuk, *Phys. Rev. E* **87**, 043109 (2013).